PHYSICAL REVIEW B **79**, 165420 (2009)

Surface geometry of Cu{531}

G. Jones,[1,*] M. J. Gladys,[1,2] J. Ottal,[1] S. J. Jenkins,[1] and G. Held[1,3,†]
[1]*Department of Chemistry, University of Cambridge, Cambridge CB2 1EW, United Kingdom*
[2]*School of Mathematical and Physical Sciences, University of Newcastle, Callaghan 2308, Australia*
[3]*Department of Chemistry, University of Reading, Reading RG6 6AD, United Kingdom*

(Received 26 December 2008; revised manuscript received 7 March 2009; published 14 April 2009)

We present a combined quantitative low-energy electron diffraction (LEED) and density-functional theory (DFT) study of the chiral Cu{531} surface. The surface shows large inward relaxations with respect to the bulk interlayer distance of the first two layers and a large expansion of the distance between the fourth and fifth layers. (The latter is the first layer having the same coordination as the Cu atoms in the bulk.) Additional calculations have been performed to study the likelihood of faceting by comparing surface energies of possible facet terminations. No overall significant reduction in energy with respect to planar {531} could be found for any of the tested combinations of facets, which is in agreement with the experimental findings.

DOI: 10.1103/PhysRevB.79.165420 PACS number(s): 68.35.B−, 68.35.Md, 61.05.jh, 71.15.Mb

I. INTRODUCTION

Chiral metal and mineral surfaces show enantioselective behavior with regard to the adsorption and reactions of organic molecules;[1–6] however the mechanisms responsible for this behavior are not very well understood on the molecular scale. The main emphasis in recent studies of intrinsically chiral substrates has been on high-Miller-index kinked surfaces of metal single crystals with cubic bulk lattice symmetry, such as Pt or Cu. If the three Miller indices h, k, l are different from each other and from zero, these surfaces have no mirror symmetry and therefore cannot be superimposed onto their mirror images, which makes them chiral substrates. It has been found that such surfaces show enantioselectivity with respect to the adsorption and reactions of chiral molecules.[7–9] In principle, the specific Miller indices (hkl) unambiguously define the chirality of a surface. For crystals with cubic symmetry it is easy to verify that a change in sign of one index, $(hkl) \rightarrow (\bar{h}kl)$, or a permutation of two indices, $(hkl) \rightarrow (khl)$, leads to the opposite chirality. Since there are only two enantiomorphs within each family of $\{hkl\}$ surfaces,[10] McFadden *et al.*[2] have introduced the notation $\{hkl\}^{R/S}$ in order to distinguish between them in analogy to chiral molecules, which was later generalized by Attard.[7] The latter notation is based on the existence of kink atoms, which are surrounded by microfacets of different atomic densities [e.g., {111}, {100}, and {110} for surfaces of face-centered-cubic (fcc) crystals]. Following these facets in order of decreasing density describes either a clockwise or anticlockwise rotation, which defines the surface chirality as "R" or "S," respectively. More recently Jenkins and Pratt suggested an alternative approach, which is based on the rotation of high-symmetry crystallographic directions around the surface normal.[11,12] This notation, using "D" and "L" instead of R and S, is also applicable to crystal structures (such as bcc) where the chiral surfaces do not have kink atoms. For fcc crystals the R surface always corresponds to the D surface and S to L; such a statement of equivalence does not hold generally for other crystal structures, where the D/L notation is preferred.

Intrinsically chiral surfaces and adsorption thereon have been studied with surface science methods in some detail mainly by scanning tunneling microscopy, photoemission spectroscopies [x-ray photoelectron spectroscopy (XPS), near-edge x-ray-absorption fine structure], IR spectroscopy, and density-functional theory (DFT) (see Refs. 5 and 13–15, and references therein). Due to the choice of experimental methods, very little is known to date about the exact geometries of chiral adsorption complexes on such surfaces although this information is crucial for the understanding of stereoselectivity in any system. For fcc transition metals, such as Cu or Pt, {531} surfaces have the smallest unit cell of all possible chiral surfaces and are therefore well suited for *ab initio* modeling and quantitative low-energy electron-diffraction intensity vs voltage (LEED-IV) structure analysis. The surface unit cell also has the right proportions to accommodate small amino acids such as alanine or glycine.[6,9] Our recent combined quantitative LEED-IV and DFT studies of Pt{531} (Refs. 16 and 17) showed that this surface does not reconstruct and has an arrangement of atoms very similar to bulk termination except for very strong inward relaxation of the kink atoms in the topmost layer. On the other hand, theoretical and experimental studies also showed that Pt{531} is thermally relatively unstable[16,18] and tends to roughen. This instability is due to the low (sixfold) coordination of the kink atoms in the topmost surface layer and the short-range bonding between Pt atoms. Cu{531} can be expected to be less affected by roughening because the long-range interaction between substrate atoms beyond the nearest neighbors is more important for Cu than for Pt atoms.

A number of studies report that medium-size chiral molecules show enantioselective behavior on chiral Cu surfaces.[6,8,9,19–25] In addition, Zhao and co-workers[26–29] showed that the adsorption of amino acids can modify the surface morphology of achiral stepped or close-packed Cu surfaces such that they expose chiral facets. The structures of several clean open Cu surfaces have been studied by LEED-IV and DFT, including {211},[30] {210},[31,32] {311},[33] {320},[34] and {532}.[35] These studies report no indications of large-scale reconstructions; however large relaxations of the under-coordinated atoms are observed in all these surfaces. STM studies of the clean chiral Cu{643} and Cu{5 8 90} surfaces[29,36] show high mobility of the Cu surface atoms but, on

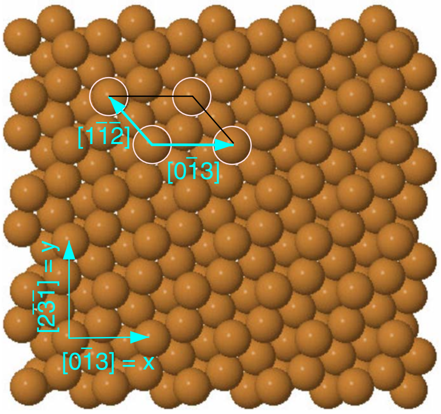

FIG. 1. (Color online) Diagram of the bulk-terminated Cu(531) (Cu$\{531\}^S$) surface indicating the main crystallographic directions, the surface unit cell ($\vec{a}_1=[0\bar{1}3]$; $\vec{a}_2=[1\bar{1}\bar{2}]$), and the coordinate system used in the LEED calculations.

average, a regular arrangement of kinks and steps is shown for {643}.

In this paper we present a quantitative LEED-IV analysis of the clean Cu{531} surface and compare the results with those of first-principles DFT calculations. Additional calculations have been performed for more close-packed surfaces that would be exposed if the {531} surface undergoes a "mesofaceted" reconstruction.[12] None of the likely combinations for faceting has been found significantly more stable than {531}.

II. EXPERIMENTAL AND THEORETICAL PROCEDURES

A. Experiment

The LEED experiments were performed in an UHV system, described elsewhere,[37] which routinely reached a base pressure in the 10^{-11} mbar range. Two Cu single crystals (from MaTecK) were used in the experiments, terminated by $\{531\}^R$ and $\{531\}^S$ surfaces[2,7] (equivalent to $\{531\}^D$ and $\{531\}^L$, respectively[11,12]), which were oriented with a precision of 0.1°; the bulk-terminated surface geometry of the *S* surface is shown in Fig. 1. The standard cleaning procedures involved repeated cycles of sputtering at room temperature and annealing in vacuum to 1000 K. Prior to that, annealing cycles in oxygen (1×10^{-7} mbar; 350–500 K) were carried out in order to remove any carbon and sulfur contaminants from the surface. Dosing of oxygen was, however, avoided in the final stage of the cleaning process since even small amounts cause significant surface faceting, which can only be removed by sputtering and high annealing temperatures >1050 K. These cleaning procedures had been established and checked by XPS in previous experiments.[9]

The UHV chamber was equipped with a computer-controlled four-grid rear-view Omicron LEED system, from which the LEED-IV data were recorded using a video-rate charge-coupled device camera. LEED images were recorded over an energy range from 15 to 300 eV in steps of 1 eV at a sample temperature of 140 K. Since there was no risk of electron-beam damage a relatively high beam current of around 1.2 μA was used. This has the advantage of a high signal-to-noise ratio and short data-acquisition times (less than 10 min). The spot intensities were extracted off line from the digitally stored LEED images using our own program MKIV.[38] This program records the intensities of all visible spots at once and determines the reciprocal lattice from their positions. Therefore, the traces of spots with low intensity are not lost even for extended "dark" periods. Finally, the IV curves were processed using Fourier transform smoothing to eliminate the high-frequency noise without affecting the significant peak structure. The cutoff frequency corresponds to features 4 eV wide. Because the Cu{531} surface has no symmetry, normal incidence cannot be found in the usual way by comparing symmetry-equivalent beams. Instead the sample was adjusted by eye close to normal incidence, and the polar and azimuthal angles of incidence were incorporated as additional search parameters in the structural analysis with starting values estimated from the spot positions in the recorded LEED images.

B. LEED calculations

The model calculations for the LEED structure determination were performed with our "CLEED" program package[39] which is an implementation of fully dynamical scattering theory based on algorithms described by Pendry[40] and Van Hove and Tong.[41] Because of the small interlayer distance of 0.61 Å, layer doubling could not be employed and the reflection matrix for the entire surface had to be calculated by using the combined space or "giant matrix inversion" method. The surface was modeled by using a stack of 16 layers (≈9 Å) after test calculations had shown that increasing the stack thickness beyond this number did not lead to significant changes in the IV curves. In earlier studies, LEED calculations using the same method and similar stack thickness for other stepped and kinked surfaces led to good agreement with experimental data.[17,42,43]

LEED intensities were calculated for electron energies between 30 and 250 eV in steps of 4 eV. The constant damping potential V_{0i} was set to 5.0 eV, which is equivalent to the inelastic mean-free path of around 5 Å in the relevant energy range. The rms thermal displacement, $\langle(\Delta r)^2\rangle$, was initially set to 0.065 Å for all Cu atoms, which is the value calculated from the bulk Debye temperature of Cu, 343 K, and the sample temperature of 140 K. In the final step of the geometry optimization the rms displacements were optimized to 0.11, 0.10, 0.09, 0.08, and 0.065 Å for the four uppermost layers (where the atoms have lower coordination) and the bulk atoms, respectively. The scattering phase shifts for the copper atoms were calculated with the program package provided by Barbieri and Van Hove.[44] Phase shifts were used up to a maximum angular-momentum quantum number $l_{\max}=7$. For the structure optimization and the determination of the angles of incidence, the downhill simplex method[45,46] was used. The convergence criterion was that the *R* factor values did not change within 1×10^{-4}. Pendry's R_P and *RR* factors[47] were used to compare experimental and theoretical IV curves in the geometry optimization, and for estimating the error margin of each geometry parameter, respectively.

TABLE I. Results of the calculation for Cu{531} and several vicinal surfaces: key details of the calculation (MPM=Monkhorst-Pack mesh; n_S/n_B=number of layers for the surface/bulk), N_{miss}=total number of missing neighbors, A_S=area of the (1×1) unit cell, γ=surface energy, $d_{n,n+1}$, d_{bulk}=interlayer distances (in Å). Comparison with experimental results from LEED-IV analysis.

Surface termination	MPM	n_S	n_B	N_{miss}	A_S/Å^2	γ/eV Å^{-2}(J m^{-2})	d_{12}	d_{23}	d_{34}	d_{45}	d_{bulk}
{111}	7×7×1	9	15	3	5.73	0.089 (1.42)	2.06 (−1%)	2.09 (+1%)	2.08 (0%)	2.09 (0%)	2.08
Expt.[a]							2.12 (+1%)				2.08
{100}	8×8×1	9	16	4	6.50	0.095 (1.52)	1.76 (−2%)	1.83 (+2%)	1.81 (0%)	1.80 (0%)	1.80
Expt.[b]							1.78 (−1%)	1.83 (+2%)			1.80
{110}	12×7×1	8	16	6	9.19	0.102 (1.63)	1.14 (−11%)	1.33 (+4%)	1.27 (0%)		1.27
Expt.[b]							1.18 (−8%)	1.31 (+2%)			1.28
{311}	10×6×1	12	22	7	10.78	0.102 (1.63)	0.94 (−14%)	1.13 (+4%)	1.08 (−1%)	1.09 (0%)	1.09
Expt.[c]							0.96 (−12%)	1.11 (+2%)			1.09
{210}	7×9×1	14	30	10	14.54	0.106 (1.69)	0.68 (−16%)	0.75 (−7%)	0.87 (+8%)	0.80 (−1%)	0.81
Expt.[d]							0.72 (−11%)	0.77 (−5%)	0.84 (+4%)		0.81
{531}	5×5×1	21	35	13	19.23	0.1065 (1.70)	(see Table II)				0.61

[a] Reference 53.

[b] Reference 54.

[c] Reference 33.

[d] References 31 and 32.

Data from 28 spots were used in the analysis. Since the surface has no symmetry, the IV curves of all spots are different from each other, which leads to a large cumulative energy range of inequivalent spots in the *R*-factor analysis. The *R* surface had sharper LEED spots whose intensities could be extracted over a wider energy range. A cumulative energy range, ΔE, of 2935 eV could be used for the structure analysis of this surface, whereas only 1454 eV could be used for the less well-ordered *S* surface. These result in *RR* factors of 10% and 14%, respectively. More details about the error estimation can be found in Refs. 17 and 47. As mentioned before, the azimuthal and polar angles of incidence could not be set with sufficient accuracy ($<0.2°$) in the experiment. These were optimized alongside the geometrical parameters in each search with starting values estimated from the recorded LEED images.

C. First-principles DFT calculations

In addition to the experiments above, the rearrangement of atoms at the Cu{531} surface was studied by means of DFT calculations using the CASTEP computer code.[48] The generalized gradient approximation as proposed by Perdew *et al.*[49] was applied (henceforth referred to as GGA-PW91) for exchange and correlation, combined with Vanderbilt ultrasoft pseudopotentials[50] for electron-ion interactions. For the clean Cu{531} surface, the plane-wave basis set was truncated at a kinetic energy of 340 eV to describe the electronic wave functions. The bulk lattice constant (a=3.606 Å) for use in the Cu surface calculations was determined with a 8×8×8 Monkhorst-Pack sampling of the bulk Brillouin zone.[51] The surface was modeled using a 35-layer bulk slab with the lower 14 layers fixed at their bulk positions and the upper 21 layers mobile. Periodic boundary conditions were used to model an extended surface. A Monkhorst-Pack mesh of 5×5×1 was used to sample the Brillouin zone. This represents a comparable depth to that used previously for eight-layer slabs on the Cu{110} surface[52] and ensures a high level of accuracy.

For comparison of surface energies and in order to estimate the likelihood of faceting reconstructions, similar calculations were also performed for Cu{111}, {100}, {110}, {311}, and {210}. For each surface a double-sided (1×1) slab was constructed. Special consideration is needed to be given to the length of the supercell employed because a bulk calculation had to be carried out in the same unit in order to keep numerical consistency in terms of *k*-point convergence, Fourier transform grid, and other computational sources of error. Therefore, the total number of atomic layers, n, in the direction of the surface normal (i.e., slab+vacuum) must be a multiple of the bulk repeat periodicity perpendicular to the $\{hkl\}$ plane, i.e., $n=m(h^2+k^2+l^2)$ ($h^2+k^2+l^2=3$ for {111}, 1 for {100}, 2 for {110}, 5 for {210}, 11 for {311}, and 35 for {531}). The surface energy, γ_{hkl}, was determined using the following equation:

$$\gamma_{hkl}=\frac{1}{2A_S}\left(\frac{n_S}{n_B}E_B-E_S\right), \tag{1}$$

where E_B and E_S are the total energies from the bulk and surface calculations, respectively, n_S and n_B are the numbers of atoms in the surface and bulk calculations, and A_S is the surface area of the (1×1) unit cell. It is not possible for each system to use the same calculation parameters; therefore each surface is treated individually and tested for convergence self consistently. Table I lists the results and the parameters used in each calculation.

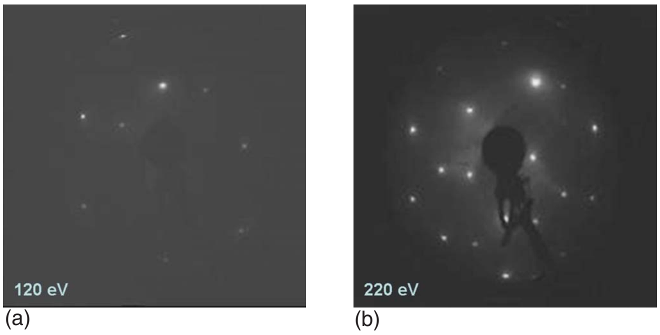

FIG. 2. (Color online) LEED pattern of the Cu$\{531\}^R$ surface at (a) 120 and (b) 220 eV.

III. RESULTS

A. LEED-IV

As mentioned above, the LEED pattern of the Cu$\{531\}^R$ surface (see Fig. 2) was significantly sharper than that of the *S* surface (not shown). Small traces of oxygen at the level of a few percent of a monolayer (ML) led to long-range faceting on both surfaces, which could be completely removed by annealing to 1050 K on the *R* surface; on the *S* surface, however, only sputtering together with annealing restored the (1×1) LEED pattern. This is most likely due to a slightly greater miscut of the *S* surface. Trace impurities other than oxygen are unlikely since both samples were cut from the same single crystal.

The main analysis was performed with the data from Cu$\{531\}^R$. The LEED spots from this surface could be tracked over a wider energy range than for the *S* surface. At the beginning of the study neither the chirality nor the absolute orientation of the surface were known. Since the positions of the LEED spots (not the intensities) have a twofold rotation symmetry, *R* and *S* surface geometries had to be tested for two orientations rotated by 180°. In all cases, the calculations were performed explicitly for the (531) (or *S*) surface as shown in Fig. 1. The theoretical IV curves were then compared with the experimental data after the relevant mirror and rotation operations were applied, as shown in Fig. 3. Starting from the bulk-terminated surface geometry, in the first step only the vertical coordinates of the atoms in the six topmost layers were optimized (together with the angles of

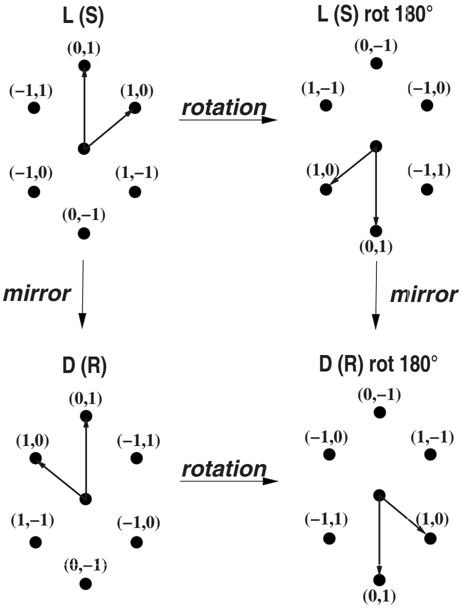

FIG. 3. Rotation and mirror operations used to compare the intensities of experimental LEED spots with those calculated for the Cu(531) (Cu$\{531\}^S$) surface.

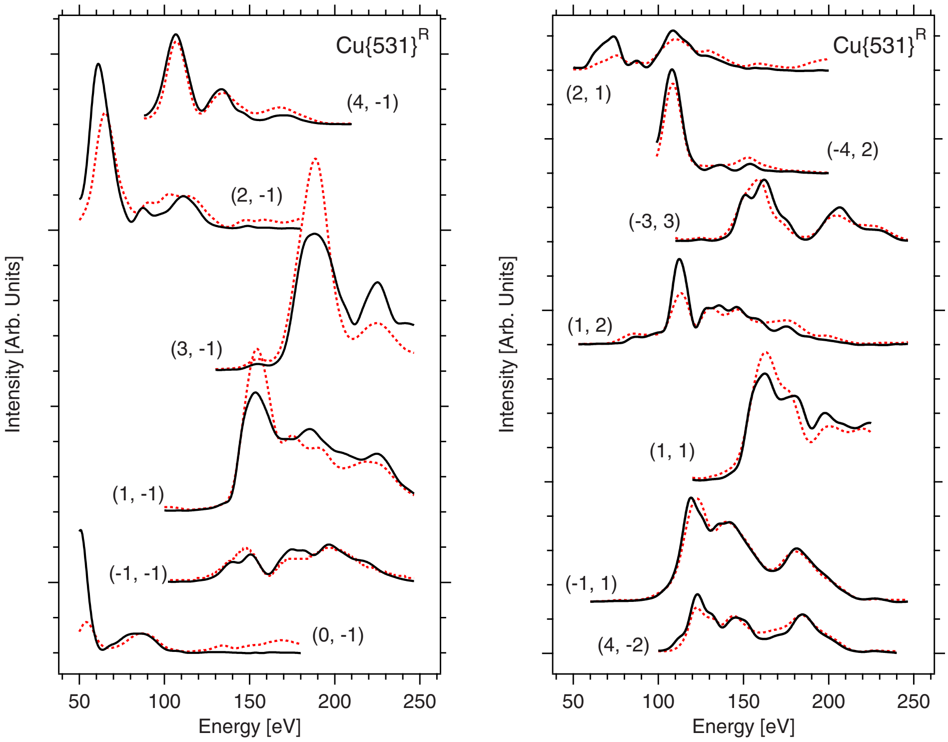

FIG. 4. (Color online) Selection of LEED-IV curves for the Cu$\{531\}^R$ surface. Experimental curves are plotted as solid, calculated curves as dotted lines.

incidence) for all four orientations shown in Fig. 3. The lowest R_P factors were 0.813 (S), 0.818 (S, rotation by 180°), 0.296 (R), and 0.826 (R, rotation by 180°). These results clearly identify the chirality and orientation of the surface. In the next step the lateral coordinates (x and y) and rms vibrational displacements of the topmost four atomic layers were optimized in addition to parameters optimized before (in total 14 geometrical parameters), which led to a final R_P value of 0.230. Calculated and experimental IV curves for a selection of LEED spots are shown in Fig. 4. The atom coordinates of the best-fit surface geometry are listed in Table II and the geometry is sketched in Fig. 5.

The best-fit geometry and rms displacements found for the R data were used as start parameters for the analysis of the data from the S surface. The same level of optimization led to a final R_P factor of 0.142, which is significantly lower than for the R data. The S data set is, however, much smaller, with many spots only contributing over a range of 50–100 eV; therefore the data analysis has a statistical error of similar magnitude as for the R surface (the RR factor is 14% for the S and 10% for R data). A comparison between calculated and experimental IV curves is shown in Fig. 6 for a selection of LEED spots. Note that the beam indices in both Figs. 4 and 6 refer to the enantiomorph, for which the calculation was explicitly performed (i.e., S); however IV curves with identical indices are still not expected to be equal because the experiments were performed for different angles of incidence.

The results of both structure determinations are listed in Table II. In general, there is very good agreement in the absolute x and y coordinates of all atoms with differences well below the statistical error bars, around 0.10 Å, which are typical for lateral coordinates in LEED. (Note that the x coordinates of the R and S surfaces have opposite signs.) The exception is the x coordinate of the Cu atom in the fourth layer, for which the difference is slightly bigger than the error bar. In relation to the relevant error bars there is a larger difference in the absolute z coordinates but if we compare relative coordinates (i.e., the vertical distance between consecutive layers, $\Delta z_{n,n+1}$, which is the quantity that predominantly influences the LEED intensities) the agreement is significantly better. All $\Delta z_{n,n+1}$ are within 0.04 Å, which is a typical error bar for vertical parameters in LEED structure determinations. Somewhat surprising is the fact that the biggest deviation is found for $\Delta z_{1,2}$, which should be the most accurate structure parameter.

B. DFT calculations, faceting

The optimized Cu{531} surface geometry resulting from the DFT calculations is also included in Table II. The agreement with the results from the LEED-IV analyses is well within the error bars of the latter; in particular, the signs of layer relaxations agree with the LEED analysis for all interlayer distances that deviate significantly from the bulk values.

Table I lists the surface energy of Cu{531} together with the energies for Cu{111}, {100}, {110}, {311}, and {210}, which are the most likely facet orientations that could be

TABLE II. Atomic positions and other relevant parameters for the best fit structures of the LEED analyses of the Cu{531} R and S surfaces, and the DFT *ab initio* calculations; rms=vibrational root-mean-square displacement, all coordinates are given in Å. The error bars were calculated using Pendry's RR method. The parameters, for which no error bars are specified, were not optimized. Note, the conversion from S to R is a mirror operation with respect to the y axis; therefore the x coordinates have opposite signs in the LEED results of the R and the S surfaces.

	Bulk termination (S)			LEED (R surface)				LEED (S surface)				DFT (S surface)			
Layer (rms)	x	y	z	x	y	z	$\Delta z_{n,n+1}$	x	y	z	$\Delta z_{n,n+1}$	x	y	z	$\Delta z_{n,n+1}$
1 (0.11)	0.00	0.00	0.00	0.01 (±0.11)	0.06 (±0.12)	−0.13 (±0.03)	0.51 (−17%)	−0.02 (±0.09)	0.04 (±0.09)	−0.07 (±0.04)	0.55 (−10%)	−0.02	−0.03	−0.18	0.51 (−16%)
2 (0.10)	2.29	0.97	−0.61	−2.31 (±0.11)	1.01 (±0.10)	−0.64 (±0.04)	0.58 (−5%)	2.26 (±0.08)	0.97 (±0.11)	−0.62 (±0.04)	0.57 (−7%)	2.26	0.98	−0.69	0.52 (−15%)
3 (0.09)	−1.14	1.93	−1.22	1.15 (±0.13)	1.99 (±0.10)	−1.22 (±0.04)	0.56 (−8%)	−1.08 (±0.07)	2.02 (±0.10)	−1.18 (±0.05)	0.59 (−3%)	−1.16	1.90	−1.21	0.59 (−3%)
4 (0.08)	1.14	2.90	−1.83	−1.13 (±0.09)	2.91 (±0.13)	−1.78 (±0.03)	0.68 (+11%)	1.03 (±0.06)	2.89 (±0.11)	−1.78 (±0.03)	0.68 (+11%)	1.08	2.89	−1.80	0.68 (+11%)
5 (0.065)	0.57	0.48	−2.44	−0.57	0.48	−2.46 (±0.04)	0.61 (+1%)	0.57	0.48	−2.46 (±0.06)	0.61 (−1%)	0.53	0.46	−2.48	0.60 (−2%)
6 (0.065)	2.86	1.45	−3.06	−2.86	1.45	−3.07 (±0.04)	0.59 (−3%)	2.86	1.45	−3.06 (±0.05)	0.60 (−1%)	2.84	1.44	−3.08	0.60 (−2%)
7(bulk) (0.065)	−0.57	2.41	−3.67	0.57	2.42	−3.67	0.61	−0.57	2.41	−3.67	0.61	−0.60	2.43	−3.68	0.60 (−1%)
8(bulk) (0.065)	4.57	−0.00	−4.28	−4.57	0.00	−4.28	0.61	4.57	0.00	−4.28	0.61	4.55	−0.01	−4.28	0.60 (−1%)
				R_P		0.232				0.142					
				Energy range		2926 eV				1454 eV					
				RR		0.10				0.14					

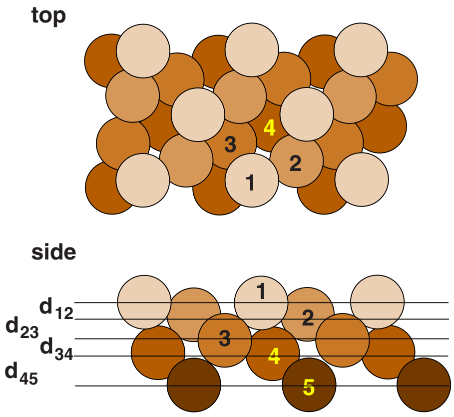

FIG. 5. (Color online) Arrangement of surface atoms in the Cu$\{531\}^S$ surface. Top and side views of best fit geometry from the LEED-IV analysis defining the geometry parameters. The numbers refer to the atomic layers with nearest-neighbor coordinations of 6 (first layer), 8 (second layer), 10 (third layer), and 11 (fourth layer).

exposed if the {531} surface undergoes a large-scale reconstruction. The total-energy differences between bulk and surface calculations (not included in Table I) scale well with the number of missing nearest-neighbor atoms per surface unit cell (about 0.16 eV per missing neighbor). Also listed in Table I are the key parameters of experimental LEED-IV structure determinations of these surfaces.[32,33,53,54] The calculated and experimental values show very good agreement, usually within a few hundredths of an Ångström, which is a typical error bar for LEED-IV results.

The surface energies of the above facets are all smaller than that of {531} but if faceting occurs the effective surface area increases, which needs to be accounted for in the energy balance. In order to predict whether a particular combination of facets would be thermodynamically favored, one has to multiply the relative surface areas and surface energies of each facet and compare these values with the surface energy of {531}. Faceting will occur if the average surface energy of the faceted surface is less than that of the unreconstructed {531} surface.

Figure 7 shows schematically one-dimensionally and two-dimensionally faceted surfaces. For a one-dimensional reconstruction, the relative areas of the two facets area(A) and area(B) on either side of the ridge scale like the lengths L_A and L_B relative to the length L_{531} parallel to the {531} plane. From simple trigonometric considerations (see the Appendix) we find that one-dimensional faceting will occur if

$$\gamma_{531} > \frac{\mathrm{area}(A)\gamma_A + \mathrm{area}(B)\gamma_B}{\mathrm{area}(AB_{531})} = \frac{\sin\beta\gamma_A + \sin\alpha\gamma_B}{\sin(\alpha+\beta)}, \quad (2)$$

or

$$\gamma_{531} > \frac{|\vec{n}_B \times \vec{n}_{531}| \cdot \gamma_A + |\vec{n}_A \times \vec{n}_{531}| \cdot \gamma_B}{|\vec{n}_A \times \vec{n}_B|}, \quad (3)$$

where $\vec{n}_A$, $\vec{n}_B$, and $\vec{n}_{531}$ are unit vectors normal to the surfaces under consideration.

Likely one-dimensional reconstructions of the (531) surface, shown in Fig. 8, contain ridges along either the $[1\bar{1}\bar{2}]$ or $[1\bar{2}1]$ directions, which are parallel to the closest-packed rows of atoms within the unreconstructed surface. The corresponding facet planes are (311)/(110) for $[1\bar{1}\bar{2}]$ and (111)/(210) or $(111)/(31\bar{1})$ for $[1\bar{2}1]$ ridges (the latter is not shown in Fig. 8). Using the above Eq. (2) or (3) we get surface energies 0.1059 eV/Å^2 for (311)/(110), 0.1062 eV/Å^2 for (111)/(210), and 0.1093 eV/Å^2 for $(111)/(31\bar{1})$ (see Table III). The first two values are only marginally smaller than

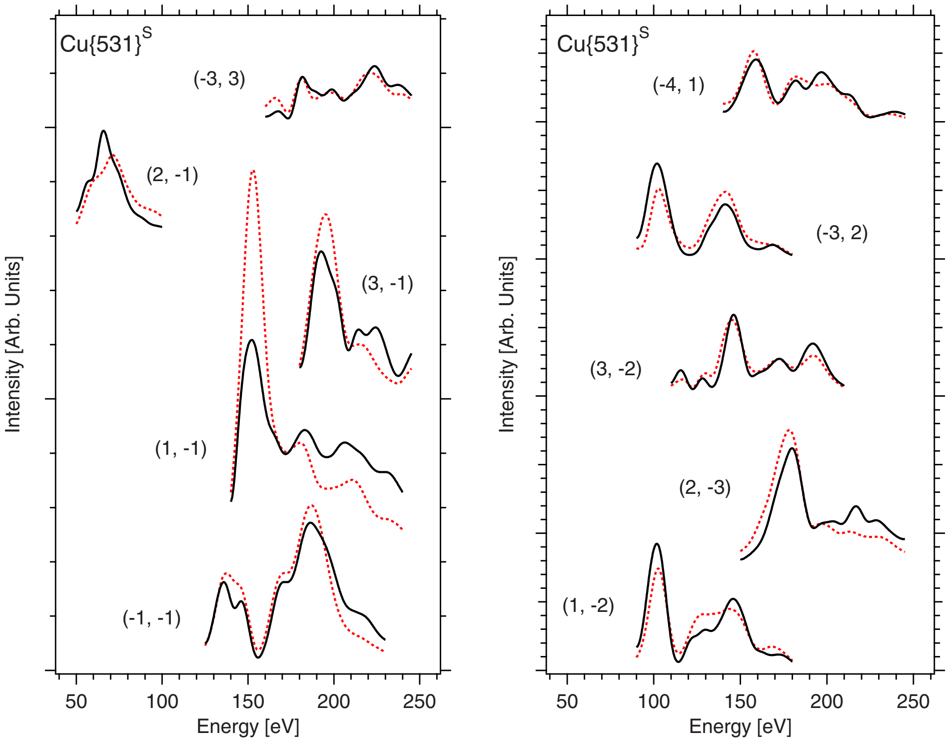

FIG. 6. (Color online) Selection of LEED-IV curves for the Cu$\{531\}^S$ surface. Experimental curves are plotted as solid while calculated curves as dotted lines.

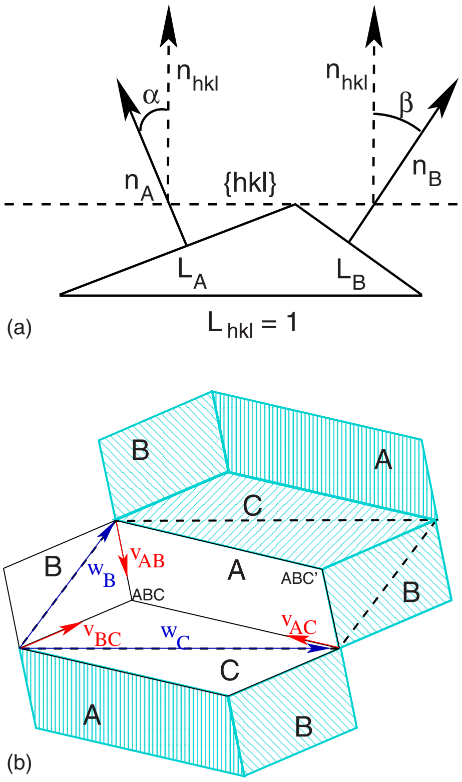

FIG. 7. (Color online) Schematic geometries of (a) one-dimensional and (b) two-dimensional faceted surfaces. See the Appendix for details.

$\gamma_{531}=0.1065\ \mathrm{eV}/\text{Å}^2$ and not outside the error margin of the calculations while faceting into $(111)/(31\bar{1})$ would lead to a significantly higher surface energy.

For a two-dimensional faceting reconstruction we get a similar condition for three facet surfaces A, B, and C:

$$\gamma_{531} > \frac{\mathrm{area}(A)\gamma_A + \mathrm{area}(B)\gamma_B + \mathrm{area}(C)\gamma_C}{\mathrm{area}(ABC_{531})}, \tag{4}$$

with the areas of the facets A, B, and C defined as

$$\mathrm{area}(A) = \frac{|(\vec{n}_C \times \vec{n}_A)\cdot\vec{n}_B|}{[(\vec{n}_C \times \vec{n}_A)\cdot\vec{n}_{531}]\cdot[(\vec{n}_A \times \vec{n}_B)\cdot\vec{n}_{531}]}, \tag{5}$$

$$\mathrm{area}(B) = \frac{|(\vec{n}_A \times \vec{n}_B)\cdot\vec{n}_C|}{[(\vec{n}_A \times \vec{n}_B)\cdot\vec{n}_{531}]\cdot[(\vec{n}_B \times \vec{n}_C)\cdot\vec{n}_{531}]}, \tag{6}$$

$$\mathrm{area}(C) = \frac{|(\vec{n}_B \times \vec{n}_C)\cdot\vec{n}_A|}{[(\vec{n}_B \times \vec{n}_C)\cdot\vec{n}_{531}]\cdot[(\vec{n}_C \times \vec{n}_A)\cdot\vec{n}_{531}]}, \tag{7}$$

and the corresponding area on the (531) surface as

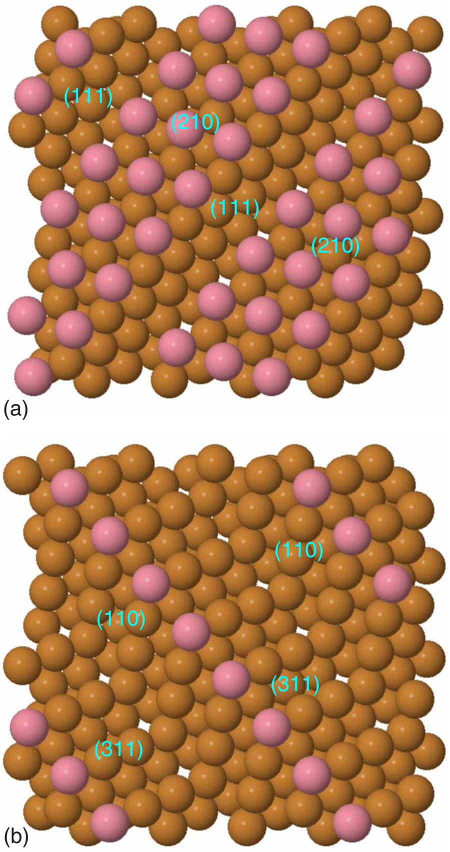

FIG. 8. (Color online) Two examples of possible one-dimensional faceting reconstructions of the Cu{531} surface. (a) (111) and (210) facets with ridges along the $[1\bar{2}1]$ direction; the top-layer atoms of the (210) facet are highlighted. (b) (311) and (110) facets with ridges along $[1\bar{1}\bar{2}]$; the ridge atoms are highlighted.

$$\begin{aligned}\mathrm{area}(ABC) = \Bigg| &\vec{n}_A \cdot \frac{[(\vec{n}_C \times \vec{n}_A)\cdot\vec{n}_B]}{[(\vec{n}_C \times \vec{n}_A)\cdot\vec{n}_{531}]\cdot[(\vec{n}_A \times \vec{n}_B)\cdot\vec{n}_{531}]} \\ &+ \vec{n}_B \cdot \frac{[(\vec{n}_A \times \vec{n}_B)\cdot\vec{n}_C]}{[(\vec{n}_A \times \vec{n}_B)\cdot\vec{n}_{531}]\cdot[(\vec{n}_B \times \vec{n}_C)\cdot\vec{n}_{531}]} \\ &+ \vec{n}_C \cdot \frac{[(\vec{n}_B \times \vec{n}_C)\cdot\vec{n}_A]}{[(\vec{n}_B \times \vec{n}_C)\cdot\vec{n}_{531}]\cdot[(\vec{n}_C \times \vec{n}_A)\cdot\vec{n}_{531}]}\Bigg|\end{aligned} \tag{8}$$

(see the Appendix, parameter a set to one). From the values in Table I the most likely faceting arrangement is $A=(111)$, $B=(100)$, and $C=(110)$. This combination of facets leads to an average surface energy of $0.1070\ \mathrm{eV}/\text{Å}^2$ for the faceted surface, which is slightly higher but again within the error margin of γ_{531}. Table III lists other possible facet combinations, which have been identified in Ref. 12. These are all significantly higher in surface energy than γ_{531}.

In the above consideration all energy contributions due to the lower coordination of atoms at facet boundaries are ignored. These will most likely further increase the energy of the faceted surfaces; we therefore conclude that "mesofac-

TABLE III. Possible faceting combinations for the (531) surface and their average surface energies; the values in brackets are the relative energy changes with respect to the unreconstructed surface; the last column "NN appr." lists the relative energy changes if calculated using the nearest-neighbor approximation (see text for details).

Facets	Angles w/r (531)	Surface area change	Surface energy/eV Å^{-2}		NN appr.
		Two-dim. faceting			
(100), (111), (110)	32.3°, 28.6°, 17.0°	+10.9%	0.1071	(+0.5%)	−2.0%
(311), (111), $(11\bar{1})$	14.5°, 28.6°, 46.9°	+14.6%	0.1093	(+2.6%)	−0.7%
(100), (111), $(11\bar{1})$	32.3°, 28.6°, 46.9°	+21.6%	0.1104	(+3.7%)	−1.8%
		One-dim. faceting			
(311), (110)	14.5°, 17.0°	+3.9%	0.1059	(−0.5%)	−0.9%
(111), $(31\bar{1})$	30.0°, 28.6°	+14.6%	0.1093	(+2.6%)	−0.7%
(111), (210)	28.6°, 10.7°	+4.9%	0.1062	(−0.3%)	−0.5%
		No faceting			
(531)			0.1065		

eted" reconstructions are energetically not favored for Cu{531}.

IV. DISCUSSION

The surface geometries of Cu{531} resulting from the LEED experiments and the *ab initio* calculations agree well, within the error bars of the LEED-IV analysis. In particular, the pattern of vertical relaxation is the same: contractions of the first three interlayer distances $\Delta z_{1,2}$, $\Delta z_{2,3}$, and $\Delta z_{3,4}$ with respect to the bulk distance of 0.61 Å, and a large expansion for $\Delta z_{4,5}$, followed by layers which are essentially bulklike. With two exceptions (layers 3 and 4 in the LEED results for the *S* surface) the lateral displacements from the bulk positions are all less than 0.1 Å, again within the error bar of the analysis. As in the case of Pt{531} (Ref. 17) the largest interlayer distance separates the undercoordinated atoms from those which are surrounded by a complete shell of 12 atoms (layers 5 and below). The same pattern of behavior was also found in the DFT study of Cu{532} by Mehmood *et al.*[35] By moving closer together, the electron density and hence the effective coordination numbers are increased for the undercoordinated atomic layers. The vertical relaxations of the Cu{531} surface atoms are between −10 to −17% ($\Delta z_{1,2}$) and +11% ($\Delta z_{4,5}$). This is similar to Cu{532} (between −17% and +24%) but significantly less than the relaxations found for Pt{531}, which range from −30/22% to +43/18% (LEED/DFT). Another important difference between the structures of these two surfaces is the fact that Pt{531} has a strong tendency to roughen, which not only affects the widths of the diffraction spots but also their IV curves.[16] Destructive interference of electron waves diffracted from atoms at different heights causes additional broad minima in the LEED-IV curves that cannot be reproduced by assuming a flat surface. Such effects have not been found for Cu{531}; the experimental IV curves agree well with those calculated for a flat surface, as can be seen in Figs. 4 and 6. This is probably also the reason for the much better agreement between LEED-IV analysis and DFT calculations that was achieved in the present study as compared to Ref. 17.

Roughening was predicted theoretically for Pt{531} by Power *et al.*,[18] using a Monte Carlo-type molecular simulations approach, and is thermodynamically favored if the change in the entropy-related contribution to the free-surface energy is greater than the energy needed to create an adatom-vacancy pair.[16] The latter can be expected to be small since both adatoms and top-layer atoms have the same coordination of nearest neighbors. (This can be shown to be a property of all kinked, and therefore all chiral fcc surfaces[11,12].) For Pt the interatomic bond is dominated by the short-range interaction of *d* electrons, which mainly affect nearest-neighbor atoms. For Cu on the other hand, *sp* electrons play a greater role in the bond and, hence, the number of next-nearest neighbors is more important, which is different for adatoms and surface layer atoms. Atomic roughening is, therefore, less likely for open Cu surfaces. If only nearest-neighbor interactions would contribute to the surface energy, one would expect ratios

$$\gamma_{111}:\gamma_{100}:\gamma_{110}:\gamma_{311}:\gamma_{210}:\gamma_{531} = 1.00:1.15:1.22:1.24:1.31:1.29 \tag{9}$$

(we also assume here that the energy contribution per missing neighbor is independent of the position of a surface atom), whereas instead the calculated values in Table I show much smaller differences with ratios

$$\gamma_{111}:\gamma_{100}:\gamma_{110}:\gamma_{311}:\gamma_{210}:\gamma_{531} = 1.00:1.07:1.14:1.14:1.19:1.20. \tag{10}$$

It is interesting to note that the bigger differences in surface energies [Eq. (9)] would tip the balance in favor of faceting for all combinations listed in Table III (the relative differences are included in the last column); however the differences with respect to the unreconstructed {531} surface are still only at the level of a few percent or of the order 10^{-3} eV Å^{-2}, which is near the level of error in our DFT calculations. The (negative) contribution of the surface entropy that leads to roughening of this surface is at a similar level and the (positive) contribution from boundary sites can also be estimated of the order 10^{-3} eV Å^{-2} (assuming facet areas around 100 nm^2 and an energy of 0.16 eV, i.e., one extra missing neighbor, per boundary site). These considerations show that the energy difference between the most likely faceting reconstructions and the unreconstructed surface are always close to zero. In this case, kinetic effects are very important and small surface modifications can tip the balance in one or the other direction. As mentioned before, even very small amounts of oxygen can induce faceting on Cu{531}. The most likely adsorption sites of oxygen atoms at small coverages are near the low-coordinated atoms at the facet boundaries[55] and could lower the surface energy contribution of these sites enough to tip the balance in favor of faceting. These observations are in line with studies of Knight *et al.*[56,57] on Cu{410} and Cu{610}, and Reinecke and Taglauer[58] on Cu{115} and Cu{119}, where large-scale oxygen-induced faceting was observed.

In view of the above considerations it is difficult to predict the nature of enantioselective effects on either Cu or Pt{531} surfaces. Small modifications of the surface energy due to the adsorption of molecules can lead to either large-scale reconstructions or stabilization of the bulk-terminated {531} surface, depending on the interaction between adsorbate and surface atoms.

V. SUMMARY

Our quantitative LEED-IV analysis and first-principles DFT study of the clean Cu{531} surface show large inward relaxations of the uppermost two layers of around 10% with respect to the bulk interlayer distance, and a similarly large expansion of the distance between the fourth and fifth layers. The latter is the first layer with the same coordination as the Cu atoms in the bulk. Additional DFT calculations have been performed to study the likelihood of faceting by comparing surface energies of possible facet surfaces. The facet combinations with the lowest surface energies are {311}/{110}, {111}/{210} (both one-dimensional faceting), and {111}/{100}/{110} (two-dimensional faceting), which are all within 1% of the calculated surface energy of Cu{531}. Faceting does not, therefore, lead to a significant reduction in surface energy (within the likely error margin of the calculations), which is in accordance with the experimental observations.

ACKNOWLEDGMENTS

The work reported here was supported by EPSRC (through Grants No. GR/S85528/01 and No. GR/S30719/01). S.J.J. thanks The Royal Society. J.O. thanks the Nuffield Foundation for an Undergraduate Research Bursary.

APPENDIX: FACETING

1. One-dimensional faceting

For a one-dimensional faceting reconstruction [see Fig. 7(a)], the relative areas of the two facets A and B on either side of the ridge scale like the lengths L_A and L_B relative to the length L_{hkl} parallel to the {*hkl*} plane of the unreconstructed surface, which can be set equal to one for simplicity. Simple trigonometric considerations lead to the conditions:

$$L_A \sin\alpha = L_B \sin\beta, \tag{A1}$$

and

$$L_{hkl} = 1 = L_A \cos\alpha + L_B \cos\beta. \tag{A2}$$

As far as thermodynamic considerations are concerned, faceting will occur if the average surface energy of the faceted surface is less than that of the unreconstructed {531} surface, hence

$$\gamma_{hkl} > L_A\gamma_A + L_B\gamma_B = \frac{\sin\beta\gamma_A + \sin\alpha\gamma_B}{\sin(\alpha+\beta)}. \tag{A3}$$

In order to arrive at an expression that depends only on the Miller indices, the sine functions can be expressed in terms of cross products between the unit vectors normal to the surfaces under consideration, $\vec{n}_A$, $\vec{n}_B$, and $\vec{n}_{hkl}$. For cubic bulk lattices

$$\vec{n}_{hkl} = \frac{1}{\sqrt{h^2+k^2+l^2}}\begin{pmatrix} h \\ k \\ l \end{pmatrix}.$$

With these the condition for faceting is

$$\gamma_{hkl} > \frac{|\vec{n}_B \times \vec{n}_{hkl}| \cdot \gamma_A + |\vec{n}_A \times \vec{n}_{hkl}| \cdot \gamma_B}{|\vec{n}_A \times \vec{n}_B|}. \tag{A4}$$

2. Two-dimensional faceting

Two-dimensional faceting of a general macroscopic (*hkl*) surface (surface normal $\vec{n}_{hkl}$) with three facet terminations, *A*, *B*, and *C*, can be described as a combination of pyramids [with apex *ABC* in Fig. 7(b)] and inverted pyramids (with minimum at *ABC*′). The facets *A*, *B*, and *C* have Miller indices $(h_A k_A l_A)$, $(h_B k_B l_B)$, and $(h_C k_C l_C)$, and surface normals $\vec{n}_A$, $\vec{n}_B$, and $\vec{n}_C$, respectively. Important for our considerations are the vectors $\vec{v}_{AB}$, $\vec{v}_{BC}$, and $\vec{v}_{AC}$ lying along the intersecting lines of *A* and *B*, *B* and *C*, and *A* and *C*, respectively [see Fig. 7(b)]. We choose that all three vectors have unit length and are pointing toward the point *ABC*, i.e., their vertical components with respect to the macroscopic (*hkl*) plane are positive, $\vec{v}_{AB}\cdot\vec{n}_{hkl} > 0$; $|\vec{v}_{AB}| = 1$. If *A*, *B*, and *C* are arranged in mathematical positive sense (counterclockwise) around the point *ABC* [as in Fig. 7(b)], these conditions are equivalent to

$$\vec{v}_{AB} = \frac{\vec{n}_A \times \vec{n}_B}{|\vec{n}_A \times \vec{n}_B|}; \quad \vec{v}_{BC} = \frac{\vec{n}_B \times \vec{n}_C}{|\vec{n}_B \times \vec{n}_C|}; \quad \vec{v}_{AC} = \frac{\vec{n}_C \times \vec{n}_A}{|\vec{n}_C \times \vec{n}_A|}. \tag{A5}$$

The intersecting lines along the facet boundaries are multiples of these vectors, i.e., $a_{AB}\cdot\vec{v}_{AB}$, $a_{BC}\cdot\vec{v}_{BC}$, and $a_{AC}\cdot\vec{v}_{AC}$. Therefore the area of each facet can be expressed through the following vector products:

$$\text{area}(A) = |(a_{AC} \cdot \vec{v}_{AC}) \times (a_{AB} \cdot \vec{v}_{AB})| = a_{AC} a_{AB} \cdot |\vec{v}_{AC} \times \vec{v}_{AB}|, \tag{A6}$$

$$\text{area}(B) = a_{AB} a_{BC} \cdot |\vec{v}_{AB} \times \vec{v}_{BC}|, \tag{A7}$$

$$\text{area}(C) = a_{BC} a_{AC} \cdot |\vec{v}_{BC} \times \vec{v}_{AC}|. \tag{A8}$$

The footprint, area(ABC), of both pyramids (i.e., upright together with inverted) with respect to the (hkl) surface is the area between the vectors $\vec{w}_B$ and $\vec{w}_C$ [dashed line in Fig. 7(b)]. $\vec{w}_C$ is the diagonal of C and can be resolved into the sum of boundary vectors between A and C, and between B and C,

$$\vec{w}_C = a_{BC} \cdot \vec{v}_{BC} - a_{AC} \cdot \vec{v}_{AC}, \tag{A9}$$

and similarly,

$$\vec{w}_B = a_{BC} \cdot \vec{v}_{BC} - a_{AB} \cdot \vec{v}_{AB}. \tag{A10}$$

The footprint area can be expressed through the vector product of $\vec{w}_B$ and $\vec{w}_C$:

$$\text{area}(ABC) = |\vec{w}_C \times \vec{w}_B|, \tag{A11}$$

hence

$$\text{area}(ABC) = |a_{BC} a_{AC} \cdot (\vec{v}_{BC} \times \vec{v}_{AC}) + a_{AB} a_{BC} \cdot (\vec{v}_{AB} \times \vec{v}_{BC}) + a_{AB} a_{AC} \cdot (\vec{v}_{AC} \times \vec{v}_{AB})|. \tag{A12}$$

(Here we have taken into account that $\vec{v}_{BC} \times \vec{v}_{BC} = 0$ and used the fact that $\vec{v}_{AC} \times \vec{v}_{AB} = -\vec{v}_{AB} \times \vec{v}_{AC}$.) Both $\vec{w}_B$ and $\vec{w}_C$ are within the (hkl) surface and must therefore be perpendicular to $\vec{n}_{hkl}$. This leads to the conditions:

$$\vec{w}_B \cdot \vec{n}_{hkl} = 0 \Rightarrow a_{BC} \cdot (\vec{v}_{BC} \cdot \vec{n}_{hkl}) - a_{AB} \cdot (\vec{v}_{AB} \cdot \vec{n}_{hkl}) = 0, \tag{A13}$$

$$\vec{w}_C \cdot \vec{n}_{hkl} = 0 \Rightarrow a_{BC} \cdot (\vec{v}_{BC} \cdot \vec{n}_{hkl}) - a_{AC} \cdot (\vec{v}_{AC} \cdot \vec{n}_{hkl}) = 0, \tag{A14}$$

which define the relationship between the prefactors a_{AB}, a_{BC}, and a_{AC}:

$$a_{AC} = \frac{(\vec{v}_{BC} \cdot \vec{n}_{hkl}) \cdot a_{BC}}{\vec{v}_{AC} \cdot \vec{n}_{hkl}}, \tag{A15}$$

$$a_{AB} = \frac{(\vec{v}_{BC} \cdot \vec{n}_{hkl}) \cdot a_{BC}}{\vec{v}_{AB} \cdot \vec{n}_{hkl}}. \tag{A16}$$

All areas only depend on one scaling parameter which we define as $a = a_{BC} \cdot (\vec{v}_{BC} \cdot \vec{n}_{hkl})$. Now the expressions for the areas can be rewritten as

$$\text{area}(A) = a^2 \frac{|\vec{v}_{AC} \times \vec{v}_{AB}|}{(\vec{v}_{AC} \cdot \vec{n}_{hkl}) \cdot (\vec{v}_{AB} \cdot \vec{n}_{hkl})}, \tag{A17}$$

$$\text{area}(B) = a^2 \cdot \frac{|\vec{v}_{AB} \times \vec{v}_{BC}|}{(\vec{v}_{AB} \cdot \vec{n}_{hkl}) \cdot (\vec{v}_{BC} \cdot \vec{n}_{hkl})}, \tag{A18}$$

$$\text{area}(C) = a^2 \frac{|\vec{v}_{BC} \times \vec{v}_{AC}|}{(\vec{v}_{AC} \cdot \vec{n}_{hkl}) \cdot (\vec{v}_{BC} \cdot \vec{n}_{hkl})}, \tag{A19}$$

$$\text{area}(ABC) = a^2 \cdot \left| \frac{(\vec{v}_{AC} \times \vec{v}_{AB})}{(\vec{v}_{AC} \cdot \vec{n}_{hkl}) \cdot (\vec{v}_{AB} \cdot \vec{n}_{hkl})} + \frac{(\vec{v}_{AB} \times \vec{v}_{BC})}{(\vec{v}_{AB} \cdot \vec{n}_{hkl}) \cdot (\vec{v}_{BC} \cdot \vec{n}_{hkl})} + \frac{(\vec{v}_{BC} \times \vec{v}_{AC})}{(\vec{v}_{AC} \cdot \vec{n}_{hkl}) \cdot (\vec{v}_{BC} \cdot \vec{n}_{hkl})} \right|. \tag{A20}$$

With the original definitions of the vectors $\vec{v}_{AB}$ etc., Eq. (A5), it is possible to express all areas only in terms of the surface normals $\vec{n}_A$, $\vec{n}_B$, $\vec{n}_C$, and $\vec{n}_{hkl}$, e.g.,

$$\text{area}(A) = a^2 \frac{|(\vec{n}_C \times \vec{n}_A) \times (\vec{n}_A \times \vec{n}_B)|}{[(\vec{n}_C \times \vec{n}_A) \cdot \vec{n}_{hkl}] \cdot [(\vec{n}_A \times \vec{n}_B) \cdot \vec{n}_{hkl}]}, \tag{A21}$$

This can be further simplified using Lagrange's formula [$a \times (b \times c) = b(ac) - c(ab)$; we use $a = (\vec{n}_A \times \vec{n}_B)$, $b = \vec{n}_B$, and $c = \vec{n}_C$], leading to the final expressions

$$\text{area}(A) = a^2 \frac{|(\vec{n}_C \times \vec{n}_A) \cdot \vec{n}_B|}{[(\vec{n}_C \times \vec{n}_A) \cdot \vec{n}_{hkl}] \cdot [(\vec{n}_A \times \vec{n}_B) \cdot \vec{n}_{hkl}]}, \tag{A22}$$

$$\text{area}(B) = a^2 \frac{|(\vec{n}_A \times \vec{n}_B) \cdot \vec{n}_C|}{[(\vec{n}_A \times \vec{n}_B) \cdot \vec{n}_{hkl}] \cdot [(\vec{n}_B \times \vec{n}_C) \cdot \vec{n}_{hkl}]}, \tag{A23}$$

$$\text{area}(C) = a^2 \cdot \frac{|(\vec{n}_B \times \vec{n}_C) \cdot \vec{n}_A|}{[(\vec{n}_B \times \vec{n}_C) \cdot \vec{n}_{hkl}] \cdot [(\vec{n}_C \times \vec{n}_A) \cdot \vec{n}_{hkl}]}, \tag{A24}$$

$$\text{area}(ABC) = a^2 \cdot \left| \vec{n}_A \cdot \frac{[(\vec{n}_C \times \vec{n}_A) \cdot \vec{n}_B]}{[(\vec{n}_C \times \vec{n}_A) \cdot \vec{n}_{hkl}] \cdot [(\vec{n}_A \times \vec{n}_B) \cdot \vec{n}_{hkl}]} + \vec{n}_B \cdot \frac{[(\vec{n}_A \times \vec{n}_B) \cdot \vec{n}_C]}{[(\vec{n}_A \times \vec{n}_B) \cdot \vec{n}_{hkl}] \cdot [(\vec{n}_B \times \vec{n}_C) \cdot \vec{n}_{hkl}]} + \vec{n}_C \cdot \frac{[(\vec{n}_B \times \vec{n}_C) \cdot \vec{n}_A]}{[(\vec{n}_B \times \vec{n}_C) \cdot \vec{n}_{hkl}] \cdot [(\vec{n}_C \times \vec{n}_A) \cdot \vec{n}_{hkl}]} \right|. \tag{A25}$$

These are entirely defined by the Miller indices of the three facets A, B, and C, and the macroscopic surface (hkl). The condition for two-dimensional faceting only depends on ratios of areas times surface energies and is therefore independent of a:

$$\gamma_{hkl} > \frac{\text{area}(A)\gamma_A + \text{area}(B)\gamma_B + \text{area}(C)\gamma_C}{\text{area}(ABC)}. \tag{A26}$$

*Present address: Johnson Matthey Technology Centre, Blounts Court, Sonning Common, Reading RG4 9NH, UK.
†g.held@reading.ac.uk

[1] G.-M. Schwab and L. Rudolph, Z. Naturwiss Med. Grundlagenforsch **20**, 363 (1932).

[2] C. F. McFadden, P. S. Cremer, and A. J. Gellman, Langmuir **12**, 2483 (1996).

[3] K. Soai, S. Osanai, and K. Kadowaki, J. Am. Chem. Soc. **121**, 11235 (1999).

[4] G. A. Attard, A. Ahmadi, J. Feliu, A. Rodes, E. Herrero, S. Blaise, and G. Jerkiewicz, J. Phys. Chem. B **103**, 1381 (1999).

[5] S. M. Barlow and R. Raval, Surf. Sci. Rep. **50**, 201 (2003).

[6] G. Held and M. J. Gladys, Top. Catal. **48**, 128 (2008).

[7] G. A. Attard, J. Phys. Chem. B **105**, 3158 (2001).

[8] J. D. Horvath and A. J. Gellman, J. Am. Chem. Soc. **123**, 7953 (2001).

[9] M. J. Gladys, A. V. Stevens, N. R. Scott, G. Jones, D. Batchelor, and G. Held, J. Phys. Chem. C **111**, 8331 (2007).

[10] The notation (*hkl*) defines one specific surface plane with surface normal parallel to the [*hkl*] direction (in the case of cubic crystal lattice); the notation {*hkl*} stands for a family of surface planes which are related to the (*hkl*) surface by the symmetry operations of the bulk lattice, which, for cubic crystal symmetries, also includes mirror operations. Hence {*hkl*} includes both enantiomorphs.

[11] S. Pratt, S. J. Jenkins, and D. A. King, Surf. Sci. **585**, L159 (2005).

[12] S. J. Jenkins and S. Pratt, Surf. Sci. Rep. **62**, 373 (2007).

[13] C. Baddeley, Top. Catal. **25**, 17 (2003).

[14] M. Ortega Lorenzo, C. J. Baddeley, C. Muryn, and R. Raval, Nature (London) **404**, 376 (2000).

[15] F. Rosei, M. Schunack, Y. Naitoh, P. Jiang, A. Gourdon, E. Lægsgaard, I. Stensgaard, C. Joachim, and F. Besenbacher, Prog. Surf. Sci. **71**, 95 (2003).

[16] S. R. Puisto, G. Held, and D. A. King, Phys. Rev. Lett. **95**, 036102 (2005).

[17] S. R. Puisto, G. Held, V. Ranea, S. J. Jenkins, E. E. Mola, and D. A. King, J. Phys. Chem. B **109**, 22456 (2005).

[18] T. D. Power, A. Asthagiri, and D. S. Sholl, Langmuir **18**, 3737 (2002).

[19] J. D. Horvath and A. J. Gellman, J. Am. Chem. Soc. **124**, 2384 (2002).

[20] J. D. Horvath and A. J. Gellman, Top. Catal. **25**, 9 (2003).

[21] J. D. Horvath, A. Koritnik, P. Kamakoti, D. S. Sholl, and A. J. Gellman, J. Am. Chem. Soc. **126**, 14988 (2004).

[22] X. Zhao, S. S. Perry, J. D. Horvath, and A. J. Gellman, Surf. Sci. **563**, 217 (2004).

[23] B. Bhatia and D. S. Sholl, Angew. Chem., Int. Ed. **44**, 7761 (2005).

[24] R. B. Rankin and D. S. Sholl, J. Chem. Phys. **124**, 074703 (2006).

[25] Y. Huang and A. J. Gellman, Catal. Lett. **125**, 177 (2008).

[26] X. Zhao, Z. Gai, R. G. Zhao, W. S. Yang, and T. Sakura, Surf. Sci. **424**, L347 (1999).

[27] X. Zhao, R. G. Zhao, and W. S. Yang, Surf. Sci. **442**, L995 (1999).

[28] X. Zhao, J. Am. Chem. Soc. **122**, 12584 (2000).

[29] X. Zhao and S. S. Perry, J. Mol. Catal. A: Chem. **216**, 257 (2004).

[30] T. Seyller, R. D. Diehl, and F. Jona, J. Vac. Sci. Technol. A **17**, 1635 (1999).

[31] Ismail, S. Chandravakar, and D. M. Zehner, Surf. Sci. Lett. **504**, L201 (2002).

[32] Y. Y. Sun, H. Xu, J. C. Zheng, J. Y. Zhou, Y. P. Feng, A. C. H. Huan, and A. T. S. Wee, Phys. Rev. B **68**, 115420 (2003).

[33] S. R. Parkin, P. R. Watson, R. A. McFarlane, and K. A. R. Mitchell, Solid State Commun. **78**, 841 (1991).

[34] Y. Tian, J. Quinn, K.-W. Lin, and F. Jona, Phys. Rev. B **61**, 4904 (2000).

[35] F. Mehmood, A. Kara, and T. S. Rahman, Surf. Sci. **600**, 4501 (2006).

[36] M. Giesen and S. Dieluweit, J. Mol. Catal. A: Chem. **216**, 263 (2004).

[37] P. Hu, C. J. Barnes, and D. A. King, Phys. Rev. B **45**, 13595 (1992).

[38] G. Held, S. Uremovic, C. Stellwag, and D. Menzel, Rev. Sci. Instrum. **67**, 378 (1996).

[39] G. Held and W. Braun, CLEED manual (unpublished), available from the authors.

[40] J. B. Pendry, *Low Energy Electron Diffraction* (Academic, London, 1974).

[41] M. A. Van Hove and S. Y. Tong, *Surface Crystallography by LEED*, Springer Series in Solid-State Sciences (Springer, Berlin, 1979).

[42] D. Kolthoff, H. Pfnür, A. G. Fedorus, V. Koval, and A. G. Naumovets, Surf. Sci. **439**, 224 (1999).

[43] M. Hirsimäki, T. Pitkänen, M. Valden, M. Lindroos, and C. J. Barnes, Surf. Sci. **454-456**, 6 (2000).

[44] A. Barbieri and M. A. Van Hove, Phase shift program package, available from http://electron.lbl.gov/software/software.html

[45] W. H. Press, B. P. Flannery, S. A. Teukolsky, and W. T. Vetterling, *Numerical Recipes in C* (Cambridge University Press, Cambridge, 1988).

[46] J. A. Nelder and R. Mead, Comput. J. **7**, 308 (1965).

[47] J. B. Pendry, J. Phys. C **13**, 937 (1980).

[48] M. Payne, M. Teter, D. Allan, T. Arias, and J. Joannopoulos, Rev. Mod. Phys. **64**, 1045 (1992).

[49] J. P. Perdew, J. A. Chevary, S. H. Vosko, K. A. Jackson, M. R. Pederson, D. J. Singh, and C. Fiolhais, Phys. Rev. B **46**, 6671 (1992).

[50] D. Vanderbilt, Phys. Rev. B **41**, 7892 (1990).

[51] H. J. Monkhorst and J. D. Pack, Phys. Rev. B **13**, 5188 (1976).

[52] G. Jones, L. B. Jones, F. Thibault-Starzyk, E. A. Seddon, R. Raval, S. J. Jenkins, and G. Held, Surf. Sci. **600**, 1924 (2006).

[53] I. Bartoš, P. Jaroš, A. Barbieri, M. A. Van Hove, W. F. Chung, Q. Cai, and M. S. Altman, Surf. Rev. Lett. **2**, 477 (1995).

[54] H. L. Davis and J. R. Noonan, Surf. Sci. **126**, 245 (1983).

[55] L. Vattuone, L. Savioa, and M. Rocca, Surf. Sci. Rep. **63**, 101 (2008).

[56] P. J. Knight, S. M. Driver, and D. P. Woodruff, Surf. Sci. **376**, 374 (1997).

[57] P. J. Knight, S. M. Driver, and D. P. Woodruff, J. Phys.: Condens. Matter **9**, 21 (1997).

[58] N. Reinecke and E. Taglauer, Surf. Sci. **454-456**, 94 (2000).